Vertical Heating Structures Associated with the MJO as Characterized by TRMM Estimates, ECMWF Reanalyses, and Forecasts: A Case Study during 1998/99 Winter

XIANAN JIANG,*,+ DUANE E. WALISER,*,+ WILLIAM S. OLSON,# WEI-KUO TAO,@ TRISTAN S. L'ECUYER,& JUI-LIN LI,+ BAIJUN TIAN,*,+ YUK L. YUNG,** ADRIAN M. TOMPKINS,++,## STEPHEN E. LANG,@@ AND MIRCEA GRECU&&

* *Joint Institute for Regional Earth System Science and Engineering, University of California, Los Angeles, Los Angeles, California*
\+ *Jet Propulsion Laboratory, California Institute of Technology, Pasadena, California*
\# *Joint Center for Earth Systems Technology, University of Maryland, Baltimore County, Baltimore, Maryland*
@ *Laboratory for Atmospheres, NASA Goddard Space Flight Center, Greenbelt, Maryland*
& *Department of Atmospheric Science, Colorado State University, Fort Collins, Colorado*
** *Division of Geological and Planetary Sciences, California Institute of Technology, Pasadena, California*
++ *European Centre for Medium-Range Weather Forecasts, Reading, United Kingdom*
@@ *Science Systems and Applications, Inc., Lanham, Maryland*
&& *Goddard Earth Sciences and Technology Center, University of Maryland, Baltimore County, Baltimore, Maryland*

(Manuscript received 23 January 2009, in final form 6 June 2009)

ABSTRACT

The Madden–Julian oscillation (MJO) is a fundamental mode of the tropical atmosphere variability that exerts significant influence on global climate and weather systems. Current global circulation models, unfortunately, are incapable of robustly representing this form of variability. Meanwhile, a well-accepted and comprehensive theory for the MJO is still elusive. To help address this challenge, recent emphasis has been placed on characterizing the vertical structures of the MJO. In this study, the authors analyze vertical heating structures by utilizing recently updated heating estimates based on the Tropical Rainfall Measuring Mission (TRMM) from two different latent heating estimates and one radiative heating estimate. Heating structures from two different versions of the European Centre for Medium-Range Weather Forecasts (ECMWF) reanalyses/forecasts are also examined. Because of the limited period of available datasets at the time of this study, the authors focus on the winter season from October 1998 to March 1999.

The results suggest that diabatic heating associated with the MJO convection in the ECMWF outputs exhibits much stronger amplitude and deeper structures than that in the TRMM estimates over the equatorial eastern Indian Ocean and western Pacific. Further analysis illustrates that this difference might be due to stronger convective and weaker stratiform components in the ECMWF estimates relative to the TRMM estimates, with the latter suggesting a comparable contribution by the stratiform and convective counterparts in contributing to the total rain rate. Based on the TRMM estimates, it is also illustrated that the stratiform fraction of total rain rate varies with the evolution of the MJO. Stratiform rain ratio over the Indian Ocean is found to be 5% above (below) average for the disturbed (suppressed) phase of the MJO. The results are discussed with respect to whether these heating estimates provide enough convergent information to have implications on theories of the MJO and whether they can help validate global weather and climate models.

1. Introduction

The Madden–Julian oscillation (MJO; Madden and Julian 1994) is the most important form of tropical subseasonal variability and its significant role in our weather and climate systems has been widely recognized (e.g., Lau and Waliser 2005; Zhang 2005). The MJO has been intimately associated with active/break modulation

Current affiliation: International Centre for Theoretical Physics, Trieste, Italy.

Corresponding author address: Dr. Xianan Jiang, Jet Propulsion Laboratory, California Institute of Technology, MS 183-501, 4800 Oak Grove Drive, Pasadena, CA 91109.
E-mail: xianan@jifresse.ucla.edu

DOI: 10.1175/2009JCLI3048.1

of the global monsoon systems (e.g., Lau and Chan 1986; Hendon and Liebmann 1990) and tropical cyclone genesis (e.g., Maloney and Hartmann 2000; Mo 2000; Higgins and Shi 2001). The influences of the MJO have also been identified over the extratropics (e.g., Weickmann 1983; Liebmann and Hartmann 1984). Additionally, the westerly wind burst and oceanic Kelvin wave activity associated with the MJO are considered to be a possible triggering mechanism for El Niño–Southern Oscillation (ENSO; e.g., Moore and Kleeman 1999; McPhaden 1999; Kessler and Kleeman 2000). Modulation of the MJO on global biological and chemical components have also been detected (e.g., chlorophyll: Waliser et al. 2005; ozone: Tian et al. 2007; aerosols: Tian et al. 2008). The quasi-periodic occurrence of the MJO provides a primary source for the predictability of tropical atmosphere on subseasonal time scales, which may bridge the forecasting gap between medium- to long-range weather forecast and short-term climate prediction (e.g., Waliser et al. 2006; Jiang et al. 2008). Therefore, the improved understanding of the fundamental features of the MJO is necessary for achieving better simulations and predictions of our global climate and weather systems.

Unfortunately, the capability of the current general circulation models (GCMs) to simulate the MJO remains limited (e.g., Slingo et al. 1996; Slingo et al. 2005; Lin et al. 2006; Kim et al. 2009). While models can have weak or even too strong intraseasonal variance, the most consistent problem is the lack of organization with the right temporal and spatial scales and propagation characteristics of the observed MJO. Meanwhile, a comprehensive theory for the MJO has been elusive, which is necessary to understand the mechanism for its eastward propagation, as well as its characteristic horizontal/vertical structures. To increase our understanding of the MJO, and help improve our modeling capability in representing it, one strategy currently adopted by the MJO research community is to more thoroughly examine the vertical structure associated with the MJO evolution by utilizing recently available remotely sensed observations, improved analyses products, and cloud-resolving models (e.g., Sperber and Waliser 2008; Waliser and Moncrieff 2008).

Because of its potentially pivotal role in the propagation and maintenance of the MJO, there is strong interest in the latent heating structures associated with the MJO. The interaction between latent heat and atmospheric circulation lies at the heart of prevailing MJO theories (Wang 2005; Majda and Stechmann 2009). The feedbacks between the latent heat and the atmospheric circulation in the free atmosphere, in the planetary boundary layer (PBL), and at oceanic surface are fundamental to the wave-conditional instability of the second kind (CISK; Lau and Peng 1987), Ekman-CISK (Wang and Rui 1990; Hendon and Salby 1994), and wind-induced surface heat exchange (WISHE; Emanuel 1987; Neelin et al. 1987) hypotheses to explain the growth rate and phase speed of the MJO. It is suggested that the slow propagation of the MJO could be attained by a specified heating maximized in the lower troposphere in multilayer models (e.g., Chang and Lim 1988; Takahashi 1987; Sui and Lau 1989). A consistent result from a full GCM study is also obtained by Tokioka et al. (1988), who introduced a threshold for convection with a minimum entrainment rate in the cumulus parameterization scheme. It is suggested that both the altitude of the maximum heating and the phase speed of simulated MJO decrease with increasing threshold. On the other hand, Cho and Pendlebury (1997) showed that an unstable large-scale mode emerges only when the heating profile is sufficiently top-heavy. This result tends to be supported by Mapes (2000), who found that unstable mode occurs when the specified heating contains a sufficient amount of the second vertical mode of the troposphere.

Based on the Tropical Ocean and Global Atmosphere Coupled Ocean–Atmosphere Response Experiment (TOGA COARE), a vertical tilt in anomalous time–height heating profiles has been identified associated with the MJO evolution (e.g., Lin et al. 2004); namely, the maximum heating first appears in the lower troposphere prior to the onset of the MJO deep convection, then shifts upward to 450 hPa during the peak of the MJO, and further shifts to 400 hPa afterward. This tilted heating structure, indicating a transition from shallow convection to midlevel congestus, then deep convection, and finally stratiform clouds during the MJO evolution, has also been indicated by other studies (e.g., Johnson et al. 1999; Kikuchi and Takayabu 2004; Kiladis et al. 2005; Schumacher et al. 2007; Benedict and Randall 2007; Chen and Del Genio 2009). Consistent with the shallow heating maximum prior to the MJO peak, enhanced low-level moisture has also been observed (e.g., Kemball-Cook and Weare 2001; Sperber 2003; Kiladis et al. 2005; Tian et al. 2006; Benedict and Randall 2007), which is generally considered as a preconditioning process for the MJO.

The recent availability of latent heating (LH) estimates based on the Tropical Rainfall Measuring Mission (TRMM; Tao et al. 2006) provide an unprecedented opportunity to investigate heating structures associated with the MJO convection. By using LH estimates based on an earlier version of a spectral latent heating algorithm (Shige et al. 2004), Morita et al. (2006) examined vertical heating structures of the MJO based on a composite analysis. In their study, two centers of maximum heating at about 3 and 7 km are found with a minimum

around the melting level. Meanwhile, a trailing heating maximum in the upper troposphere is also exhibited to the west of MJO convection center, consistent with previous findings.

In the present study, vertical heating structures associated with the MJO are further investigated by utilizing the latest versions of TRMM estimates produced by three research groups, two latent and one radiative heating estimate. Meanwhile, heating structures derived based on the 40-yr European Centre for Medium-Range Weather Forecasts (ECMWF) Re-Analysis (ERA-40) as a residual term in the thermodynamic equation, as well as outputs from the ECMWF Integrated Forecast System (EC-IFS) at the 24-h forecast are also analyzed to facilitate a comparison to their satellite-based counterparts. Because of the limited period of data available at the time of this study, we will mainly focus on the analyses during the period of October 1998 to March 1999. A more comprehensive analysis of the heating structures for the MJO life cycle will be conducted in a follow-up study based on extended period of datasets. The organization of this paper is as follows: The datasets employed in this study are described in section 2. In section 3, we present the seasonal climatology of the heating structures over the global tropics based on both the TRMM estimates and two ECMWF model systems (hereafter EC models for brevity). Then the temporal variability of the heating structures, as well as partition of total rainfall into convective and stratiform components during the winter of 1998/99, is demonstrated in section 4. Finally, a summary and a discussion of the principal findings are given in section 5.

2. Data and approach

The two TRMM LH products employed in this study are based on ''trained'' radiometer heating (TRAIN; Grecu and Olson 2006; Grecu et al. 2009) and the convective–stratiform heating (CSH; Tao et al. 1993b, 2000, 2001) algorithms. The former utilizes both TRMM precipitation radar (PR) and microwave imager (TMI), while the latter only uses the PR. Note that the variable estimated by the TRAIN algorithm is $Q_1 - Q_R$ (hereafter TRMM/TRAIN $Q_1 - Q_R$), while that by the PR-based CSH is Q_1 (hereafter TRMM/CSH Q_1), which are defined in the following:

$$Q_1 = \underbrace{\frac{L_v}{C_p}(c-e) + \frac{L_f}{C_p}(f-m) + \frac{L_s}{C_p}(d-s)}_{\text{Term I}} + \underbrace{\pi\left(-\overline{\mathbf{V}'\cdot\nabla\theta'} - \frac{1}{\rho}\frac{\partial\rho\overline{w'\theta'}}{\partial z}\right)}_{\text{Term II}} + Q_R, \qquad (1)$$

where Q_1 is the apparent heat source following Yanai et al. (1973), while Q_R is the radiative heating rate. The primes indicate deviations from the large-scale environment due to small-scale cloud processes. The variable θ is potential temperature, ρ is air density, $\pi = (p/1000)^{R/C_P}$ is nondimensional pressure (where p is pressure in hPa), and C_p and R are the specific heat at constant pressure and gas constant of dry air, respectively. The variables L_v, L_f, and L_s are the latent heats of condensation, freezing, and sublimation, respectively, while the variables c, e, f, m, d, and s denote rates of condensation, evaporation, freezing, melting, deposition, and sublimation, respectively. Term I in Eq. (1) represents the latent heat due to phase changes, and term II is the vertical and horizontal eddy sensible heat flux convergence.

It is noted that both TRMM/TRAIN $Q_1 - Q_R$ and TRMM/CSH Q_1 are not estimated under conditions of zero surface rainfall. As a result, the radiative cooling effect during nonrainy days could be largely underestimated in both TRMM heating estimates. Therefore, in order to facilitate a more direct comparison between these two products, net radiative heating rate (Q_R) from the hydrologic cycle and earth's radiation budget (HERB) algorithm (hereafter TRMM Q_R; see L'Ecuyer and Stephens 2003, 2007; L'Ecuyer and McGarragh 2009) is used to obtain an equivalent Q_1 by adding TRMM Q_R to both TRMM/TRAIN $Q_1 - Q_R$ and TRMM/CSH Q_1. In the case of TRMM/TRAIN, adding Q_R results in a direct estimate of Q_1. In the case of TRMM/CSH, since the radiative effects over precipitating regions have been considered, only Q_R averaged over the nonrainy pixels within the grid box are added to account for the radiative heating over nonrainy regions, which was not included in the original estimate. In the following discussion, unless indicated otherwise, we use the terms TRAIN Q_1 and CSH Q_1 to denote these derived equivalent Q_1 fields based on original TRAIN $Q_1 - Q_R$ and CSH Q_1 datasets.

Another caveat in both TRMM LH estimates is that the eddy sensible heat flux convergence [term II in Eq. (1)] is not estimated in nonprecipitating regions. Since the precipitation only occupies a small fraction of a given large-scale region, the boundary layer heating due to eddy sensible heat fluxes near the earth's surface is largely missed. Fortunately, the mean boundary layer heating near the equator is typically less than 1 K day^{-1} on a global basis (e.g., Peixoto and Oort 1992) and dies off quickly from the surface upward. Nevertheless, these caveats in the TRMM estimates need to be kept in mind in the following discussions.

All the original TRMM products, TRMM/CSH Q_1, TRMM/TRAIN $Q_1 - Q_R$, and TRMM Q_R have horizontal resolutions of $0.5° \times 0.5°$ and are vertically interpolated to 18 pressure levels between 1000 and 100 hPa

from their original z levels between the surface and 18 km with 1-km resolution. Additionally, contributions to the total Q_1 by convective and stratiform components are also provided by the TRMM/TRAIN estimates. Meanwhile, the corresponding rain rate field for each LH estimate and the standard version of TRMM rainfall (version 3B42; Huffman et al. 2007) are also analyzed to interpret the difference in the LH estimates.

Heating products generated by rerunning EC-IFS (version CY31r1, http://www.ecmwf.int/research/ifsdocs/CY31r1/index.html; also see a brief description in Li et al. 2007) in hindcast mode, including its contributions by convective and stratiform latent heating, as well as sensible and radiative heating. (Unfortunately, precipitation data were not saved in these hindcasts.) EC-IFS Cy31r1 was operational between 12 September 2006 and 5 June 2007; it is also the version used in the interim reanalysis and the current seasonal forecasting system at ECMWF (Bechtold et al. 2008). The data assimilation system of the IFS uses a four-dimensional variational analysis approach with a 12-h assimilation window (Rabier et al. 1998). This employs simplified physics in the tangent linear model (Mahfouf 1999; Janiskova et al. 2002), which for cloud processes is based on a simple saturation adjustment scheme combined with the cloud scheme of Slingo (1987). The dataset employed in this study is derived from a 24-h forecast using the full nonlinear forecast model, which uses a cloud scheme based on Tiedtke (1993).

The Q_1 estimates are also derived indirectly based on ERA-40 reanalysis (Uppala et al. 2005) as heat budget residuals with profiles of temperature and the three-dimensional wind vectors (Yanai et al. 1973). Rainfall outputs based on ERA-40 reanalysis with convective and stratiform components are also examined to interpret the difference between model and TRMM estimates. The horizontal resolution of the EC-IFS dataset is $1° \times 1°$ and $2.5° \times 2.5°$ for ERA-40 reanalysis; both ECMWF datasets are interpolated to 12 pressure levels between 1000 and 100 hPa.

All the above variables are available at daily intervals during the period 1 October 1998 to 31 March 1999. Since the focus of this study is on the subseasonal variability of heating structures associated with the MJO convection, and because of missing data in the daily TRMM products due to sensor/swath sampling characteristics, all the datasets are subject to a 5-day averaging for the analyses in the following sections.

3. Seasonal climatology of vertical heating structures

Figure 1 illustrates pressure–longitudinal structures of seasonal mean (October 1998–March 1999) total heating Q_1 along the global tropics (10°S–10°N) based on two ECWMF and two TRMM estimates. The longitudinal distribution of seasonal mean rainfall averaged between 10°S and 10°N corresponding to each heating product (except for EC-IFS, in which the rainfall data was not available in the "special" hindcast run) and TRMM 3B42 are also displayed in Fig. 1e. Evident in all datasets (Figs. 1a–d) is the strong heating rate with maximum height between 400 and 600 hPa over the eastern Indian Ocean/western Pacific sector, the eastern Pacific and Atlantic Oceans, and continental areas of Africa and South America. The large rainfall amounts over these regions as shown in Fig. 1e are consistent with strong heating in the atmosphere, indicating dominant role of LH to the total Q_1 (e.g., Tao et al. 1993a; Olson et al. 1999). It is noted that the mean heating patterns in the two EC models bear larger amplitudes than those by TRMM estimates. This could be related to the model biases in the precipitation in the two EC models as indicated by the green curve in Fig. 1e based on the ERA-40 reanalysis. Also discernible is that the heating structures in the EC models exhibit a deeper vertical extent, stretching over the entire troposphere. In contrast, cooling in the lower troposphere is evident based on both TRMM estimates.

It is particularly noteworthy that a layer with shallow heating between 800 and 600 hPa is noticed over the central-eastern Pacific in the TRMM/TRAIN Q_1 estimate (Fig. 1c), which may reflect the presence of shallow trade wind cumulus in this region. As noted by Grecu et al. (2009), however, shallow convective heating in the eastern Pacific may be overestimated by the TRMM/TRAIN algorithm, since this heating appears to be weaker in fields derived from the PR training algorithm. This also explains why the shallow heating is not evident in the PR-based TRMM/CSH Q_1 estimate (Fig. 1d), as the weak heating structure over the eastern Pacific in the original TRMM/CSH Q_1 estimate is dominated by the radiative cooling effect when deriving the equivalent Q_1 pattern. Note that the shallow heating is also discernible within the PBL in the two EC models.

It is also worth mentioning that the differences in the mean heating structures in the PBL based on the two EC models and two TRMM estimates could be partially due to the lack of the eddy sensible heat flux divergence component [term II in Eq. (1)] over nonprecipitating regions in the TRMM estimates as previously mentioned. While the amplitude of the PBL heating due to the eddy sensible heat fluxes over clear-sky regions is generally thought to be small over the tropical regions, this effect needs to be further investigated in the future study. Moreover, Q_1 estimates over land areas based on the TRMM/CSH algorithm should be regarded with caution. Since flat terrain is adopted in the current

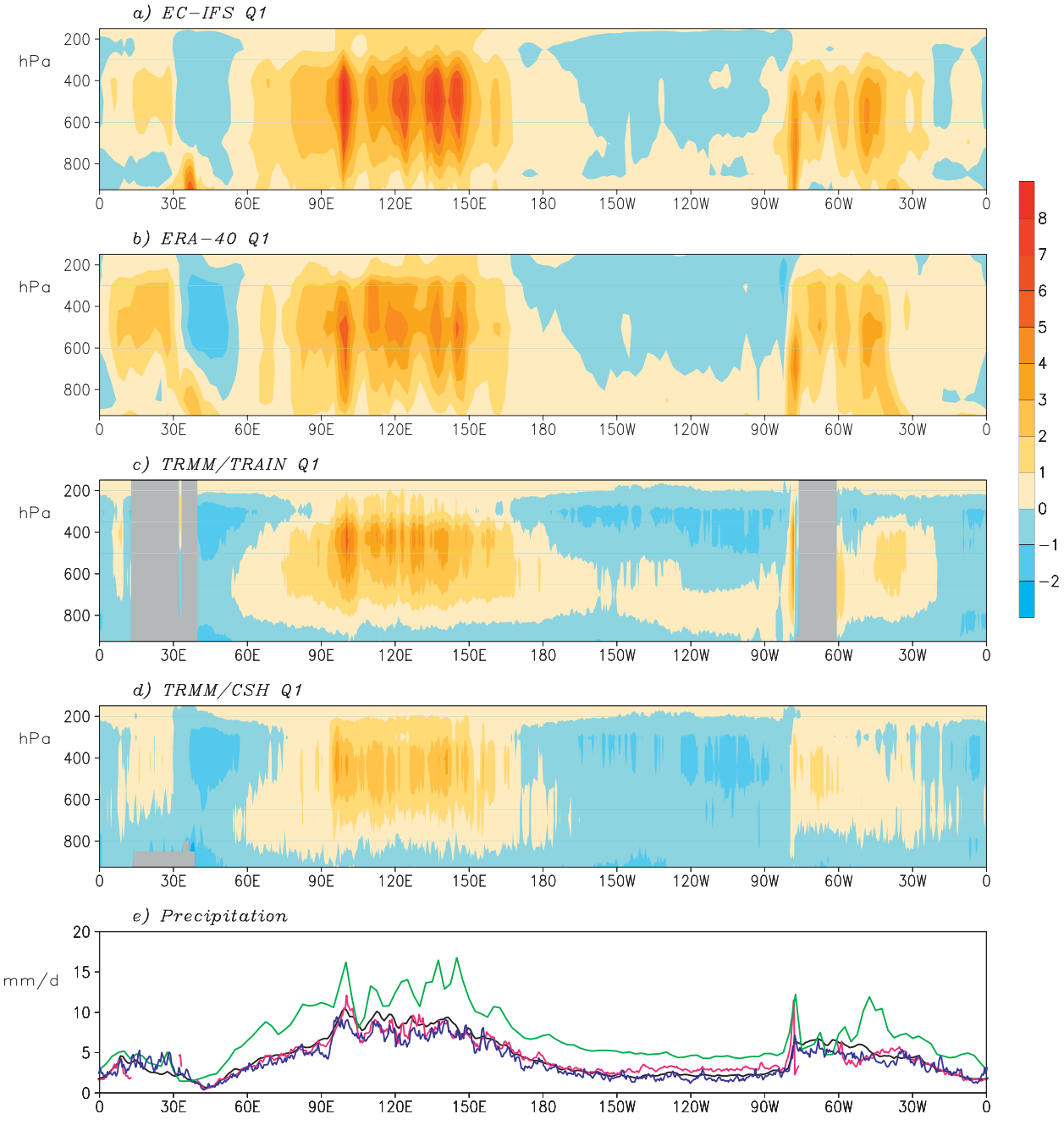

FIG. 1. Longitude–pressure distribution of seasonal mean Q_1 (K day^{-1}) based on (a) EC-IFS 24-h forecast, (b) ERA-40 reanalysis, (c) TRMM/TRAIN algorithm, and (d) TRMM/CSH algorithm. (e) Longitudinal distribution of seasonal mean rainfall (mm day^{-1}) based on various datasets: TRMM 3B42 (black), ERA-40 (green), TRMM/TRAIN (red), TRMM/CSH (blue). The seasonal mean is calculated from October 1998 to March 1999. All variables are averaged over equatorial zone between 10°S and 10°N.

cloud-resolving model, which is used to generate lookup tables that both TRMM LH schemes depend heavily on, the altitudes of maximum heating in the TRMM/CSH Q_1 will be artificially lowered over the land region. The TRMM/TRAIN algorithm is not applied over the land surfaces, since microwave latent heating signatures are compromised by the strong microwave emission from land surface. This issue will not seriously affect the analyses in this study, since our main focus is on the equatorial oceanic regions.

In Fig. 2, the variability of total Q_1 (Figs. 2a–d) and rainfall (Fig. 2e) over the global tropics (averaged over

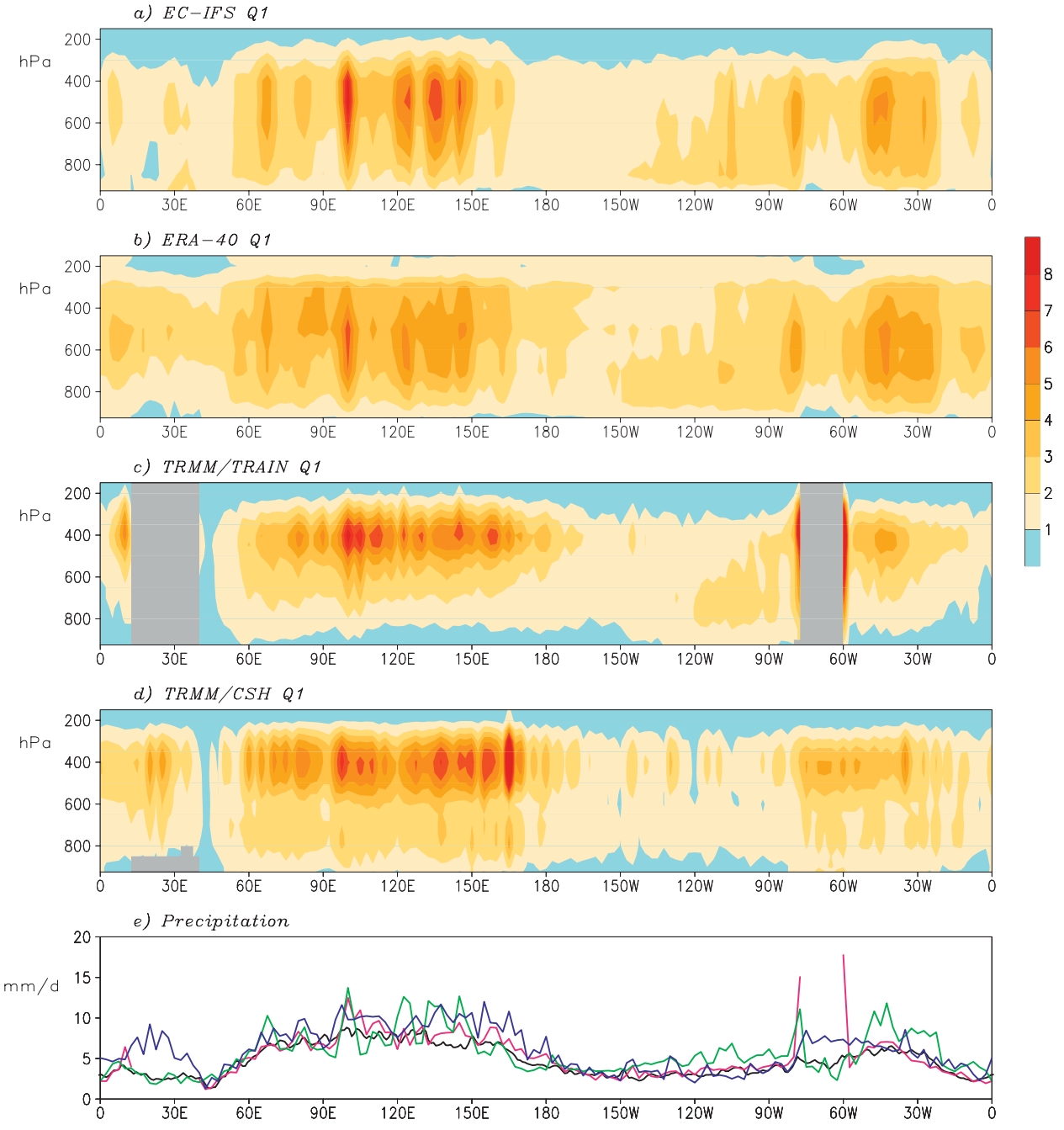

FIG. 2. As in Fig. 1, but for standard deviations of Q_1 and rain rate.

10°S–10°N) are displayed via their standard deviations during the 1998/99 winter season based on pentad mean data.[1] In contrast to their relatively large amplitudes in the seasonal mean structures (Figs. 1a,b), heating patterns based on two EC models display slightly weaker variability compared to the TRMM estimates in general. This is particularly obvious in the ERA-40 reanalysis over the western Pacific as will be further displayed in the following. The maximum variability centers in the EC models are found near 500 hPa, while they are located at about 400 hPa in the two TRMM estimates.

[1] To eliminate the potential influences of the horizontal resolution on the standard deviations, both heating and rainfall based on all these datasets have been interpolated into the same 2.5° × 2.5° grid system when calculating the standard deviations.

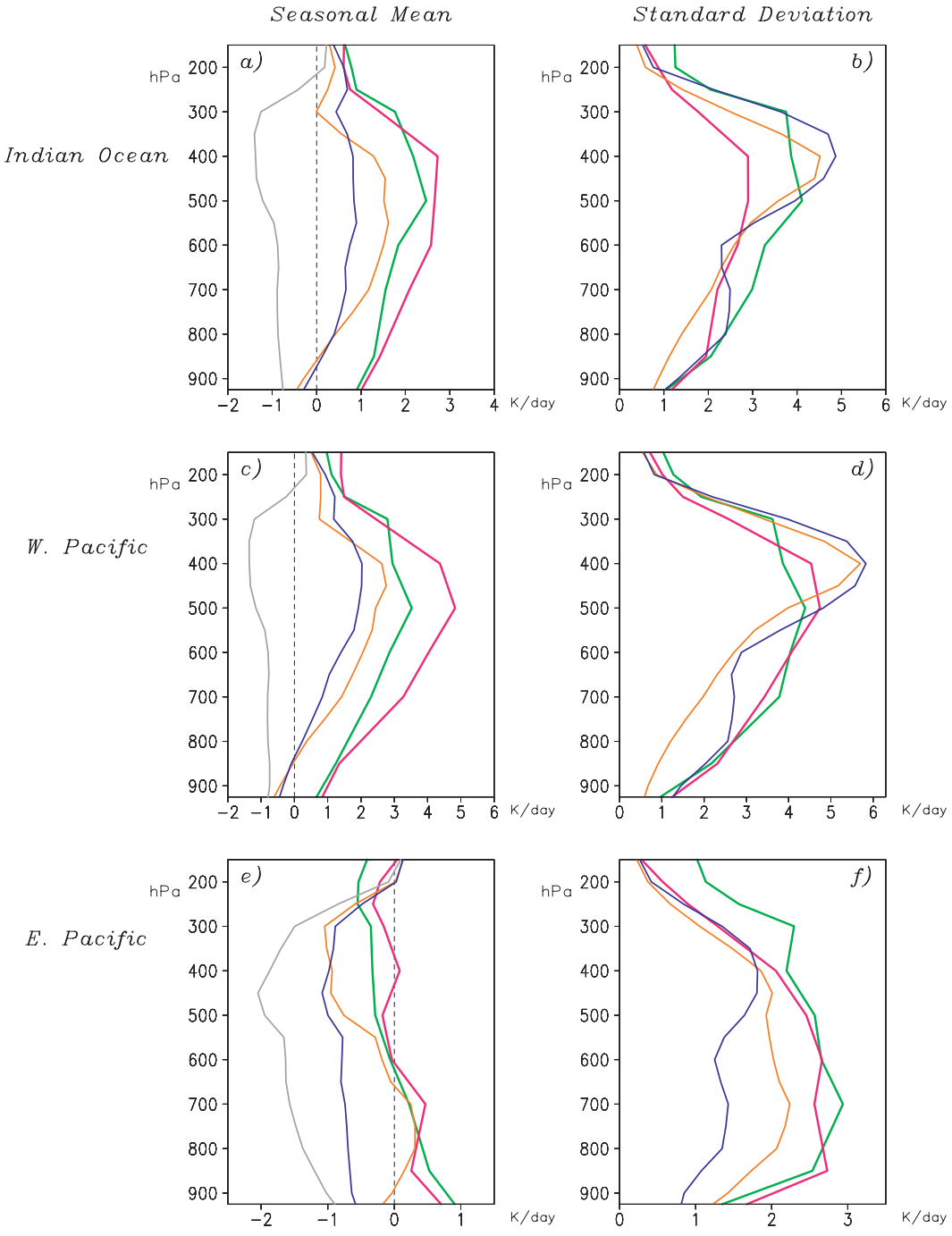

FIG. 3. Vertical structures of (left) seasonal mean and (right) standard deviation of Q_1 (K day^{-1}) during 1998/99 winter over (a),(b) the equatorial eastern Indian Ocean (10°S–10°N, 75°–85°E); (c),(d) the western Pacific (10°S–10°N, 120°–160°E); and (e),(f) the eastern Pacific (10°S–10°N, 240°–280°E) based on EC-IFS forecast (red), ERA-40 reanalysis (green), TRMM/TRAIN (orange), and TRMM/CSH (blue) estimates. Gray curves in (left) represent seasonal mean profiles of TRMM Q_R (K day^{-1}) over these above regions.

These aforementioned differences in heating structures over various datasets are further demonstrated by Fig. 3, which shows the vertical profiles of seasonal mean and standard deviations of Q_1 over the eastern equatorial Indian Ocean (EEIO; 10°S–10°N, 75°–85°E; Figs. 3a,b), the western Pacific (10°S–10°N, 120°–160°E; Figs. 3c,d), and the eastern Pacific (10°S–10°N, 120°–80°W; Figs. 3e,f). Figure 3a shows the vertical structures of

mean Q_1 in the EEIO. Clearly evident is a simple deep mode of heating rate stretching over the entire troposphere based on the two EC estimates, while weak cooling is found in the PBL in both TRMM estimates. Again, this could be partially due to the missing eddy sensible heat flux term in clear-sky regions in the two TRMM estimates as previously mentioned. The amplitudes of the maximum heating based on two EC models are much stronger than those in the TRMM estimates by a factor greater than 2. In fact, a very weak amplitude is especially evident in the TRMM/CSH Q_1 profile.

The vertical profiles of heating variability over the EEIO are illustrated by Fig. 3b. The results clearly suggest that, although the seasonal mean heating profiles in the two EC products show much stronger amplitudes than those in TRMM estimates, they exhibit relatively weaker amplitudes in their standard deviations. The maximum variability centers in both EC models appear around 500 hPa. However, maximum centers at about 400 hPa are clearly evident in both the TRMM estimates. A second variability peak around 750 hPa is also discerned in the TRMM/CSH Q_1 estimate. The difference in the heating variability at the low level between the two TRMM estimates could be associated with differences in their schemes for shallow convection and the percentages of stratiform rainfall in two algorithms, which needs to be further investigated.

The seasonal mean and standard deviations of the heating structures over the western Pacific (Figs. 3c,d) largely resemble their counterparts in the EEIO; that is, the two EC models produce much stronger amplitudes (by a factor of 2) in the seasonal mean heating structures and relatively weaker heating variability than those based on TRMM estimates. This notion is consistent with the report of relatively weak tropical wave activity, including Kelvin waves and the MJO, in this version of the EC-IFS (Cy31r1; Bechtold et al. 2008). These model deficiencies in representing the tropical wave activities are significantly improved in a recent version of EC-IFS (Bechtold et al. 2008). Larger amplitudes of the climatological mean heating profiles in the tropics based on the ERA-40 reanalysis compared to those obtained by the TRMM estimates are also reported by Chan and Nigam (2009), in which heating profiles generated by TRMM/CSH algorithm are compared to those derived from the National Centers for Environmental Prediction–National Center for Atmospheric Research (NCEP–NCAR) and ERA-40 reanalyses. The mean vertical heating maximum around 450 hPa over the western Pacific as illustrated by both of TRMM estimates is largely consistent with previously results derived from the sounding observations over the TOGA COARE region (e.g., Lin and Johnson 1996; Lin et al. 2004).

Over the eastern Pacific (Figs. 3e,f), the vertical profiles of the seasonal mean and standard deviations of total heating Q_1 exhibit very different characteristics compared to those over the EEIO/western Pacific sectors. In contrast to a maximum heating rate between 400 and 600 hPa over the EEIO and western Pacific, a cooling rate prevails above 600 hPa over the eastern Pacific based on all datasets (Fig. 3e). The amplitudes of the upper-level cooling rate are much stronger in the TRMM estimates than those in the EC models. Notable differences in heating profiles are evident below 600 hPa among various products; while the two EC products display a positive heating rate below 600 hPa, a deep cooling structure throughout the troposphere is exhibited in the TRMM/CSH estimate. The TRMM/TRAIN estimate exhibits a similar heating rate between 800 and 600 hPa as in the two EC models, except that a very weak cooling is present near the surface. The heating estimates based on all datasets exhibit maximum variability around 700 hPa over the eastern Pacific (Fig. 3f), which is in stark contrast to those over the EEIO/western Pacific (Figs. 3b,d). The heating variability based on the two EC models displays stronger amplitude than those based on two TRMM estimates. It is also noted that two variability peaks in the vertical—one at 450 hPa, the other around 750 hPa—are evident in the two TRMM estimates.

4. Subseasonal variability of latent heating

a. Overview of 1998/99 MJO activity

In this section, we will focus on heating structures associated with the MJO convection. First, to illustrate a general picture of the MJO activity during the 1998/99 winter season, a Hovmöller diagram of rainfall based on TRMM 3B42 (10°S–10°N average) is presented in Fig. 4a. A similar plot based on rainfall anomalies, where the seasonal mean values have been removed, is also displayed in Fig. 4b to demonstrate clearer propagating features of the MJO. It is readily seen that there are three strong MJO events during this winter season, which are characterized by eastward propagation of rain events from the Indian Ocean sector to western Pacific. Since the strongest MJO-like rainfall variability, with systematic eastward propagation, is observed over the EEIO, we will mainly focus on this region and proceed to inspect characteristics of the heating structures associated with these events.

b. Variability of heating structures associated with the MJO

Figure 5 illustrates time evolution of vertical Q_1 structures over the EEIO (10°S–10°N, 75°–95°E) based on the four datasets. The time evolution of corresponding

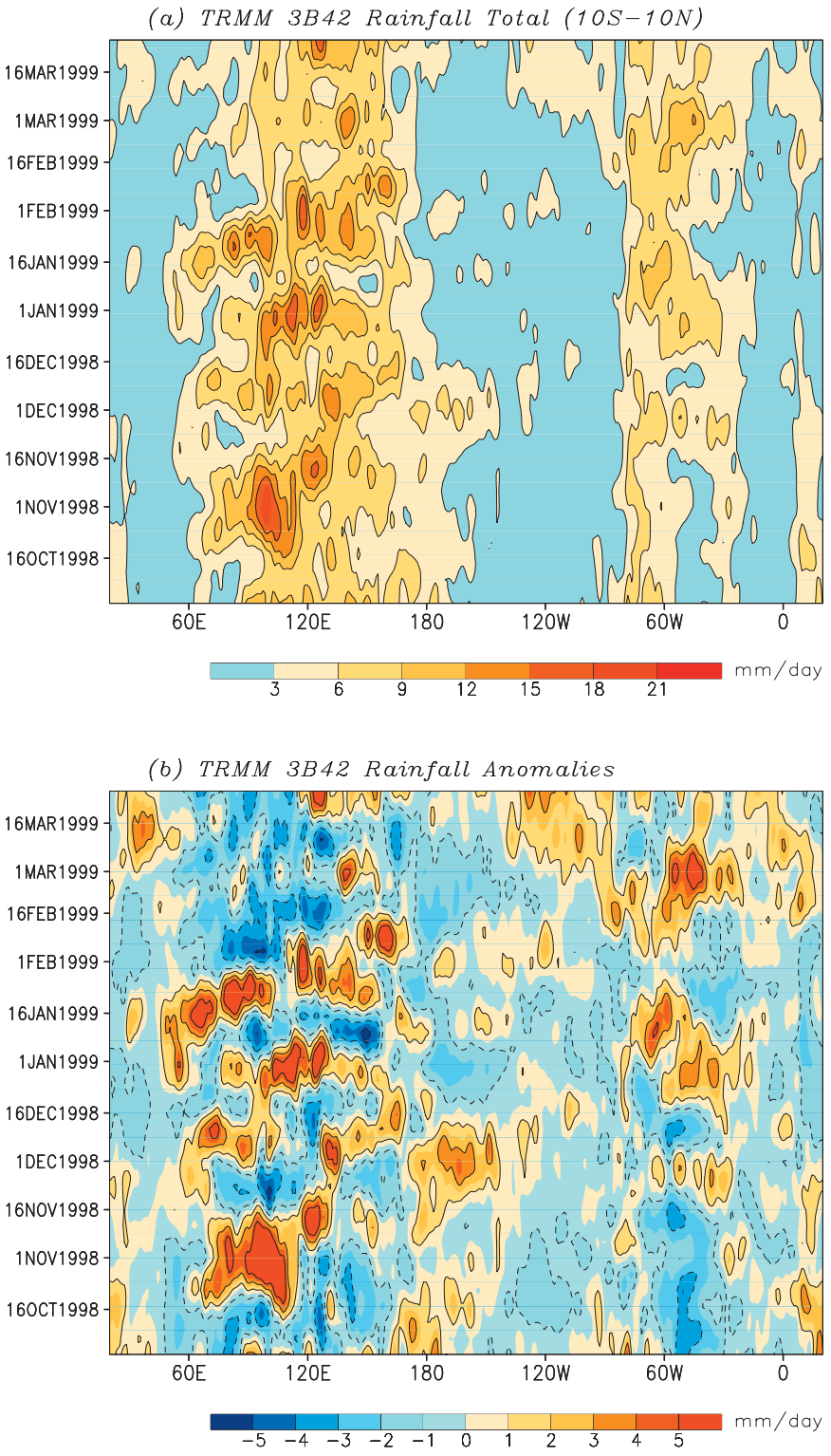

FIG. 4. Hovmöller diagram of TRMM 3B42 rainfall (averaged over 10°S–10°N; mm day^{-1}) during 1998/99 winter based on (a) total field and (b) rainfall anomalies subject to the removal of seasonal mean values. The seasonal mean rainfall is calculated based on the period of October 1998–March 1999.

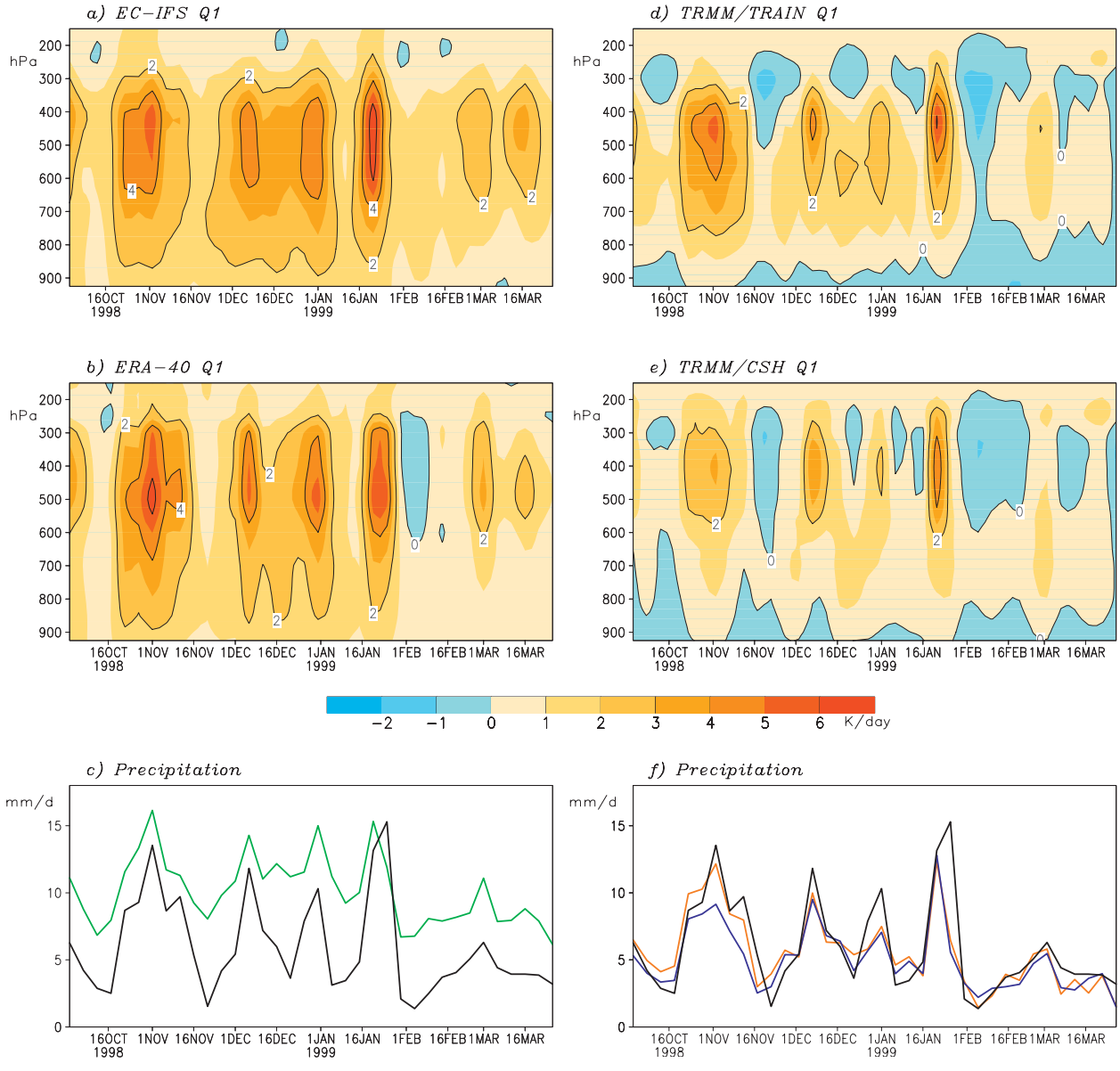

FIG. 5. Time–pressure Q_1 structures (K day^{-1}) during the 1998/99 winter based on (a) EC-IFS forecast, (b) ERA-40 reanalysis, (d) TRMM/TRAIN, and (e) TRMM/CSH estimates. (c),(f) Time evolution of rainfall (mm day^{-1}) based on various datasets: TRMM 3B42 (black), ERA-40 (green), TRMM/TRAIN (orange), and TRMM/CSH (blue). TRMM 3B42 rainfall is duplicated in (c) and (f) as a reference. All heating and rainfall fields are averaged over the equatorial eastern Indian Ocean (10°S–10°N, 75°–95°E) and are based on 5-day mean data.

rainfall fields is also displayed in two lower panels. The modulation of rainfall associated with the MJO is readily discerned in both TRMM rainfall estimates (Fig. 5f) and ERA-40 reanalysis (Fig. 5c). Corresponding to the passage of eastward-propagating MJO events over the EEIO during this period, there are five enhanced rainfall phases with intervals at subseasonal time scale as shown by TRMM 3B42 rainfall (black curve in Fig. 5c). Note that the second and third rainfall peaks during December 1998 are related with the same MJO event with some high-order modes embedded. The fifth rainfall peak around 1 March 1999, which is very weak, is not associated with pronounced eastward-propagating MJO signals in rainfall (see Fig. 4). The two other TRMM rainfall estimates display similar features as exhibited by the 3B42 (Fig. 5f). The rainfall in ERA-40 reanalysis exhibits greater mean amplitude than the TRMM estimates (Fig. 5c), in agreement with the feature previously

mentioned in the seasonal mean pattern of Fig. 1e. Nevertheless, the MJO signals can still be identified in the rainfall variation based on the ERA-40 reanalysis.

Consistent with the rainfall evolution, the vertical heating structures also display strong subseasonal variations associated with the MJO events in all four datasets. Evident is the much stronger amplitudes in the Q_1 patterns based on the two EC products than in the TRMM estimates (cf. Figs. 5a,b and Figs. 5d,e), which is also consistent with results previously discussed in the seasonal mean pattern (Fig. 3a). It is noted that positive heating prevails during most of the 6-month period in the EC models regardless of the MJO phases. In contrast, diabatic cooling is evident in a large portion of troposphere during the undisturbed phases of the MJO, and it is also dominant in the PBL in both of TRMM estimates. This PBL cooling is associated with both radiation and stratiform cloud processes below the melting level as to be shown later. Additionally, the maximum heating centers tend to appear in the middle troposphere around 500 hPa in the two EC models, while peak heating is located slightly higher in the TRMM estimates, for example, around 450 hPa in TRMM/TRAIN Q_1 and 400 hPa in TRMM/CSH Q_1.

Considering the large differences in amplitudes of heating patterns in various datasets, it is instructive to compare anomalous heating patterns based on these datasets by removing their corresponding seasonal mean values. Figure 6 illustrates similar time–pressure profiles of Q_1 over the EEIO based on the four datasets as Fig. 5, but for anomaly patterns. Anomalous rainfall evolution based on various datasets is also displayed in the lower two panels as in Fig. 5. Intriguingly, the results suggest that anomalous heating structures based on various datasets exhibit greater similarity to each other than those based on the total fields (cf. Fig. 6 and Fig. 5), including the amplitudes and vertical structures, although slight differences in the position of vertical heating maxima can still be discerned. Comparable amplitudes and evolution of the anomalous rainfall evolution from these datasets is illustrated in the lower two panels in Fig. 6, consistent with the anomalous vertical heating structures. These results suggest that the differences in the total heating structures between the four datasets as presented in Fig. 5 are mainly due to systematic biases in their means. This also explains the better agreement in the standard deviation profiles based on various datasets than in the seasonal mean profiles over the EEIO and the western Pacific warm pool region (Figs. 3b,d).

To further understand the difference of the heating structures between the EC models and TRMM estimates, contributions to total heating Q_1 due to convective, stratiform, and radiative processes are further analyzed based on the TRMM estimates and EC-IFS output. Figures 7a,d demonstrate vertical–temporal structures of the convective heating in the EC-IFS model and TRMM/TRAIN Q_1 estimates. The MJO modulation of convective heating is evident in both datasets. It is readily noticed that the amplitude of the convective heating in the EC-IFS model is much stronger than that of TRMM estimates. The vertical maxima of convective heating in both the EC model and TRMM/TRAIN estimate are evident in the midtroposphere between 500 and 600 hPa. While the convective heating structure is mainly confined between 850 and 400 hPa in the TRMM estimate, it displays a very deep extension from lower to upper troposphere in the EC-IFS model.

The stratiform heating components in both datasets, as shown in Figs. 7b,e, display a vertical dipole structure with heating in the upper troposphere and cooling at low level as suggested by previous studies (e.g., Houze 1982). This dipole pattern in the stratiform heating profile associated with the MJO events in the EC-IFS model output, however, is not as well organized as in the TRMM estimates. Generally, the upper-level heating component around 400 hPa associated with deposition of saturated air in decks of stratiform cloud is weaker in the EC-IFS model; while cooling below the 0°C level due to the melting and evaporation of precipitation appears to be stronger in the EC-IFS model.

It is noteworthy that stratiform heating component tends to be nearly in the same phase with convective heating based on both EC-IFS and TRMM estimates as shown in the pressure–time heating profiles in Fig. 7. Since the total Q_1 is largely dominated by these two components for tropical convection, the vertical tilting in the heating structures associated with the MJO over the TOGA COARE region as suggested by Lin et al. (2004) and Kiladis et al. (2005) is not very evident over the EEIO in the results presented here. Nevertheless, some weak tilting signals in the heating structures can still be discerned in Figs. 5 and 6; for example, those associated with the convective activities around 1 November and 1 December 1998 and 15 January 1999. This will be further discussed later.

Next, heating components due to net radiative processes (including longwave and shortwave radiation) based on both the EC-IFS model (Fig. 7c) and the TRMM estimates (Fig. 7f) are displayed. Generally, radiative processes lead to cooling in the troposphere as evident in both datasets. It is noteworthy that the radiative cooling rate is weaker during convectively active phases of the MJO than during suppressed MJO phases. This is particularly true in the lower troposphere (below 500 hPa). During convectively active phases of the MJO, the radiative cooling rate is about 0.5 K day^{-1}, while it is

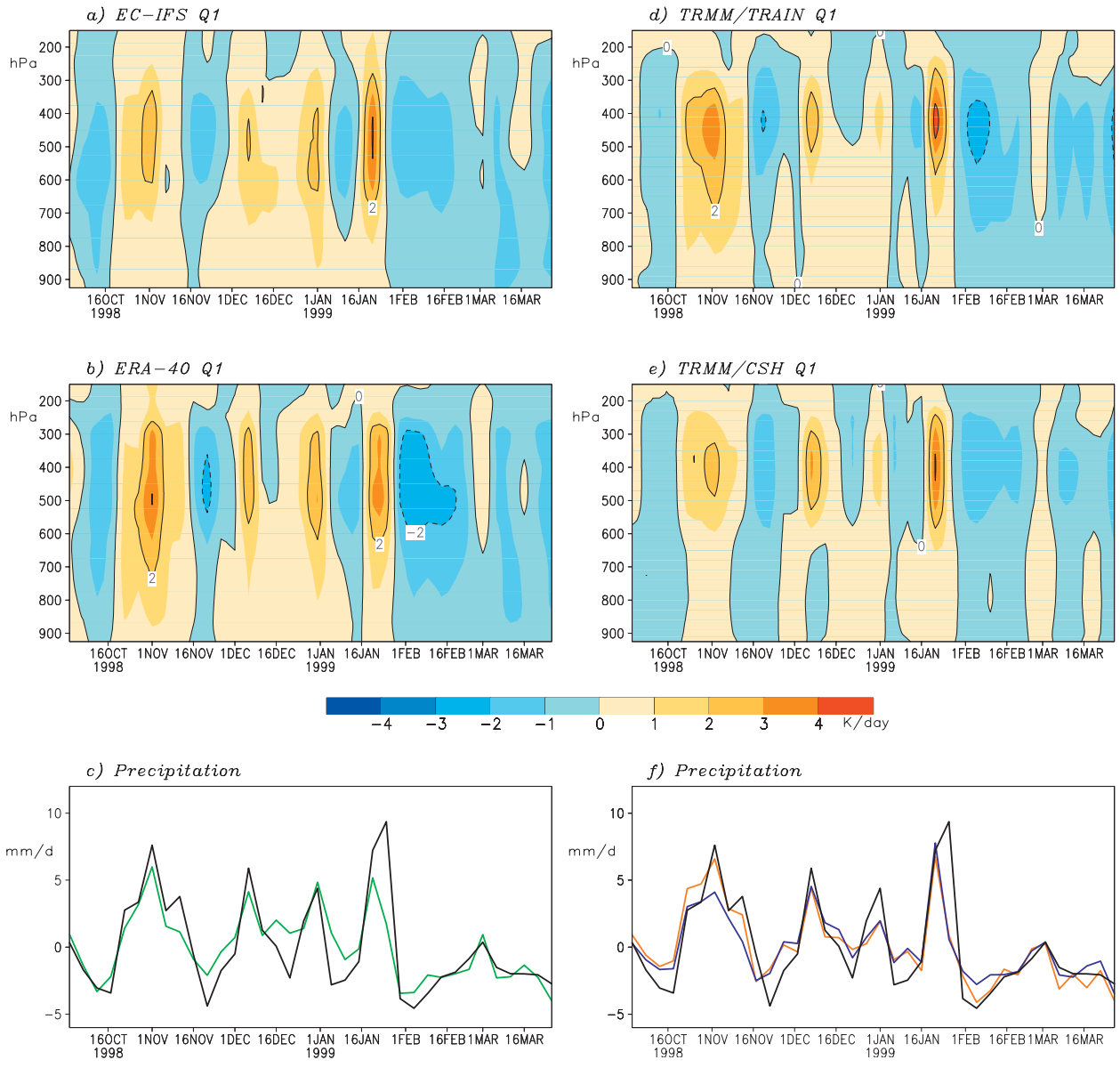

FIG. 6. As in Fig. 5, but for anomalies of the heating and rainfall fields where their corresponding seasonal mean values during the period of October 1998–March 1999 are removed.

about 1.5 K day^{-1} during convectively inactive phases of the MJO. The large variations in tropospheric radiative cooling could be a result of the atmospheric longwave cloud radiative forcing due to high cloud variations associated with the MJO (e.g., Tian et al. 2001; Tian and Ramanathan 2002; Lin et al. 2004).

To summarize, compared to the TRMM estimates, the EC-IFS model exhibits much stronger and deeper convective heating structures. Meanwhile, it shows weaker stratiform heating in the upper troposphere around 400 hPa. As a result, the total Q_1 structure, which is largely determined by the combination of these two terms, displays a heating maximum around 500 hPa in the EC-IFS model (Fig. 5a), while it is evident around 450 hPa in the TRMM estimates (Fig. 5d). Regardless of the significant difference in the total heating structures between EC models and TRMM estimates, the anomalous heating profiles based on these datasets exhibit reasonable agreement with each other.

c. *Subseasonal variability of stratiform rainfall partition*

The aforementioned differences in heating components based on the EC models and the TRMM estimates

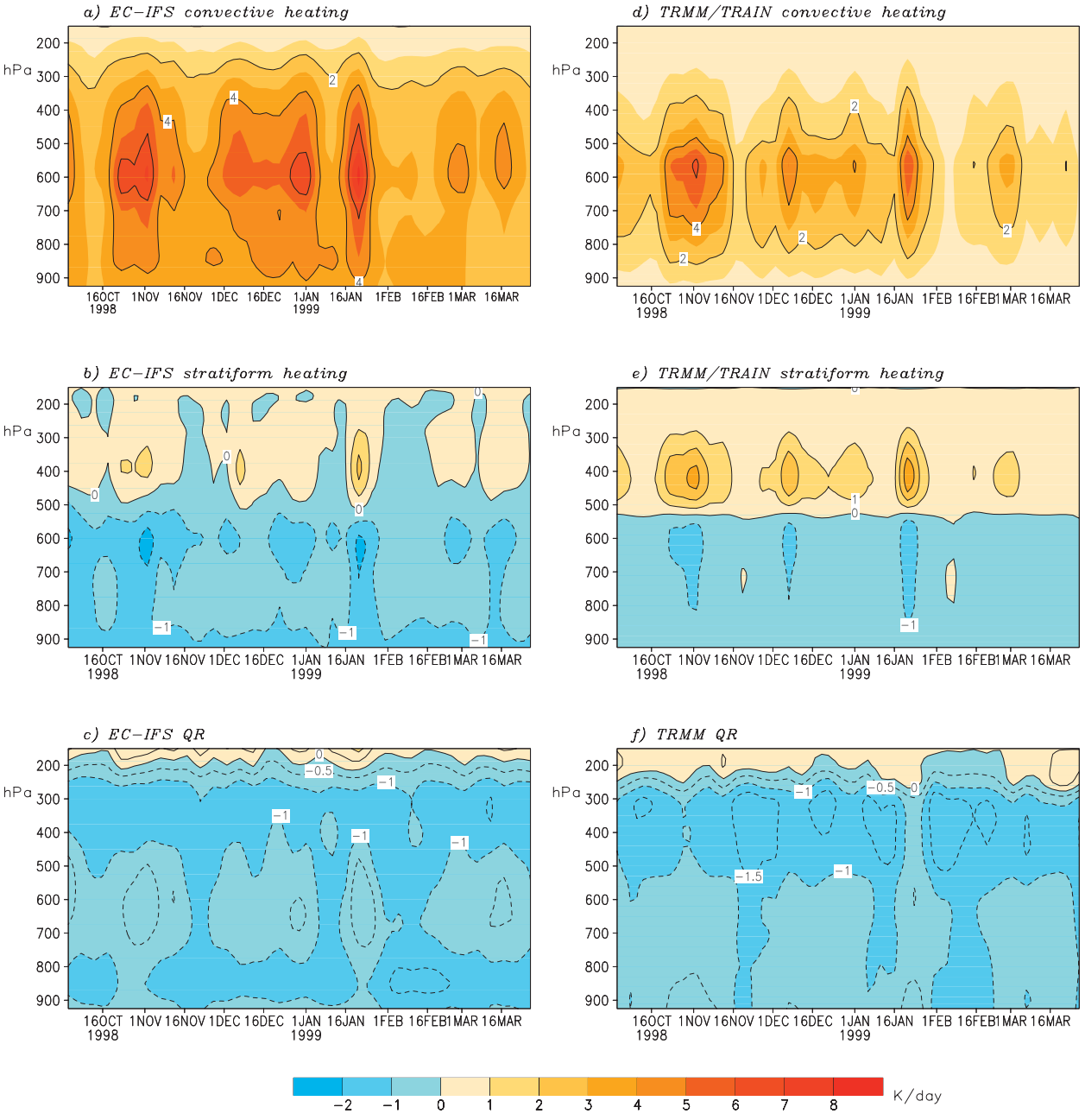

FIG. 7. Time–pressure distributions of total heating Q_1 contributed by (a),(d) convective; (b),(e) stratiform; and (c),(f) radiative components based on (left) EC-IFS forecast and (right) TRMM/TRAIN estimates. All variables are averaged over the equatorial eastern Indian Ocean (10°S–10°N, 75°–95°E; K day^{-1}). Note that contour intervals of convective and stratiform heating in (a),(b),(d), and (e) are 1 K day^{-1}, while those for radiative heating in (c) and (f) are 0.5 K day^{-1}.

could also be reflected in the partitions of convective–stratiform rain rates in these datasets. Previous studies (e.g., Lin et al. 2004; Morita et al. 2006), suggested that the stratiform rain fraction during the MJO active phase is about 10% larger than its climatological mean value in the EEIO and western Pacific. In this subsection, we examine the modulation of the convective–stratiform rain rate by the MJO based on estimates by the TRMM/TRAIN algorithm and ERA-40 reanalysis.

Figure 8 displays the time evolution of total rain rate as well as its convective and stratiform components over the EEIO during the 1998/99 winter season based on both the ERA-40 (Fig. 8a) and TRMM/TRAIN estimate (Fig. 8b). Note that the evolution of total rain rate

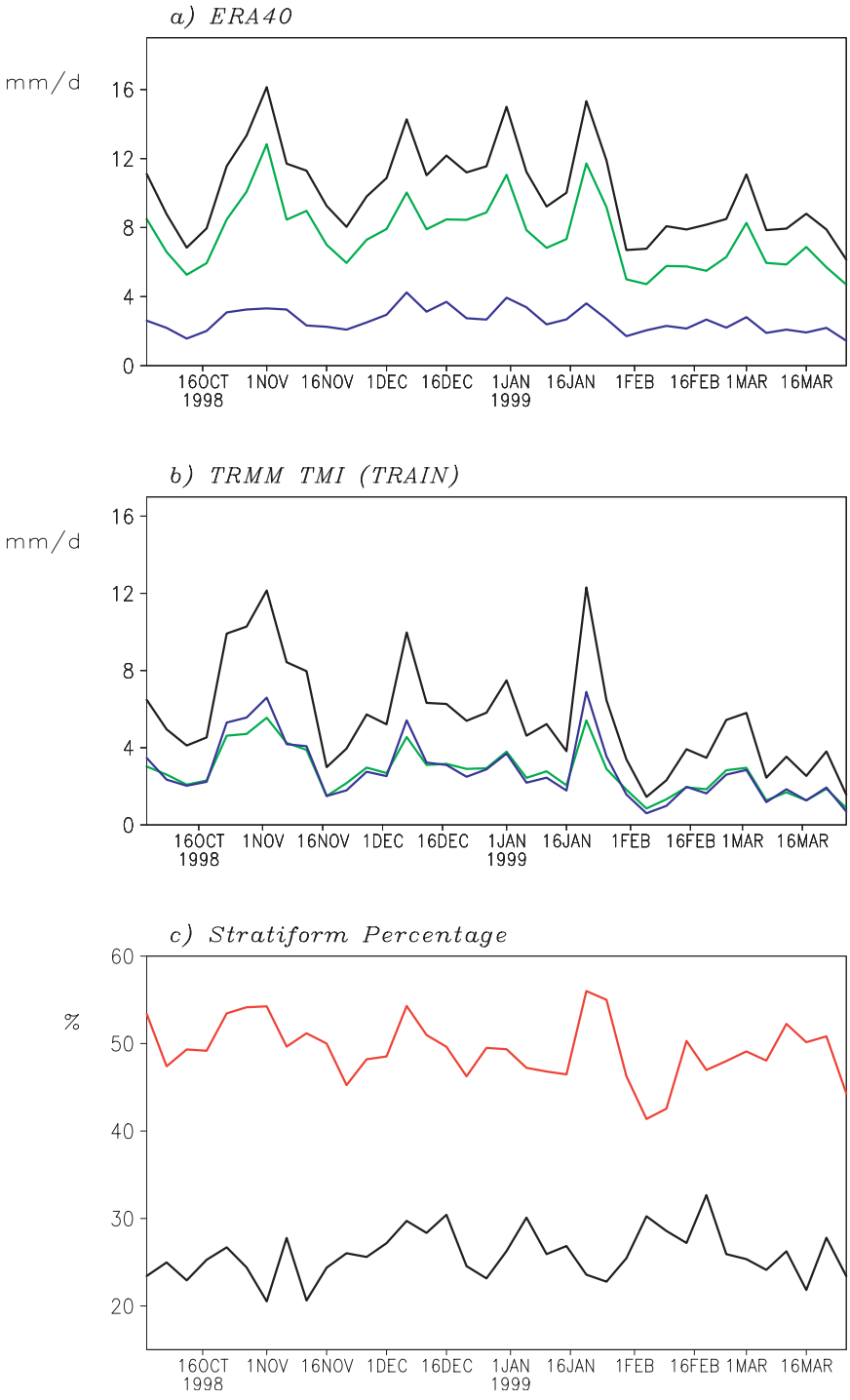

FIG. 8. Time evolution of total rain rate (black) and its convective (green) and stratiform (blue) components based on (a) ERA-40 reanalysis and (b) TRMM estimates with TRAIN algorithm during October 1998–March 1999 (units: mm day^{-1}). (c) Time evolution of stratiform rain fractions (%) based on ERA-40 reanalysis (black) and TRMM/TRAIN estimate (red). All variables are averaged over equatorial eastern Indian Ocean (10°S–10°N, 75°–95°E).

in each panel is identical to that displayed in Figs. 5c,f. The results in Fig. 8a indicate that the total rainfall is dominated by the convective component in ERA-40 reanalysis, with strong (weak) modulation of the convective (stratiform) component by the MJO. In contrast to the ERA-40 reanalysis, the TRMM/TRAIN-estimated convective and stratiform rain rates make comparable contributions to the total rain rate, and both are markedly modulated by the MJO.

To further elucidate the above point, the time evolution of the percentage of stratiform rainfall in the total rainfall over the EEIO based on both the ERA-40 reanalysis (black curve) and TRMM/TRAIN estimate (red curve) is displayed in Fig. 8c. Clearly evident is the much smaller ratio of stratiform rain rate to the total rainfall in the ERA-40 reanalysis (~25%) than that in the TRMM estimate (~50%). As the importance of stratiform rainfall for the MJO and tropical wave activities has been emphasized (e.g., Mapes 2000; Kuang 2008; Fu and Wang 2009), the smaller contribution from the stratiform rainfall component in the EC models could be a possible reason for the relatively weak tropical wave activity in earlier versions of the EC models (Bechtold et al. 2008). Meanwhile, it is interesting to note that the time evolution of the stratiform partition ratio based on the TRMM estimate corresponds well to the total rainfall variation. Namely, during enhanced (suppressed) convective phase of the MJO, the partition of stratiform rain rate tends to be increased (decreased). The range of the percentage ratio is between about 45% and 55%. Although this range of stratiform rain ratio variation associated with the MJO is slightly weaker than those reported by Lin et al. (2004) and Morita et al. (2006), the results presented in this study are generally consistent with these previous studies.

To consider the above issues across the entire tropics, Fig. 9 shows Hovmöller diagrams of total rain rate (averaged over 10°S–10°N), as well as its convective and stratiform parts, based on both the ERA-40 reanalysis and the TRMM/TRAIN estimate. The eastward propagation of the MJO convection along the equator is discernible in ERA-40 rainfall (Fig. 9a) although not very well organized. As previously mentioned, the propagating signals of the MJO in the ERA-40 dataset are mainly reflected in the convective rainfall (Fig. 9b). The stratiform rain in the ERA-40 reanalysis shows much weaker amplitudes and the eastward propagation is not very apparent (Fig. 9c). In contrast, the major eastward-propagating MJO events during the 1998/99 winter season are much better defined in total rainfall evolution based on TRMM/TRAIN estimates (Fig. 9e), as well as in both its convective (Fig. 9f) and stratiform components (Fig. 9g). Particularly noteworthy is that strong eastward-propagating signals can also be detected in the stratiform rainfall percentage diagram based on TRMM estimates (Fig. 9h), while they are not present in ERA-40 reanalysis (Fig. 9d). Also note that, while ERA-40 shows much lower stratiform percentages over the EEIO and western Pacific than those based on TRMM/TRAIN estimates, it displays much larger stratiform fraction over the eastern Pacific (cf. Figs. 9d,h). This could also be partially related to slightly smaller stratiform rain fraction over the eastern Pacific by TRMM/TRAIN estimates as compared to that by the PR training algorithm (Grecu et al. 2009).

5. Discussion and conclusions

In the present study, the diabatic heating profiles associated with the MJO during the winter of 1998/99 are examined by utilizing the latest versions of the TRMM heating estimates based on the TRAIN and CSH algorithms, in conjunction with a TRMM-based radiative heating estimate. The corresponding heating structures based on outputs from the EC-IFS as well as that derived based on the ERA-40 reanalysis are also analyzed. The analyses suggest that seasonal mean diabatic heating profiles in the two EC models exhibit much stronger amplitudes and deeper structures than those based on the TRMM estimates over the EEIO and western Pacific. The heating maxima tend to appear around 500–550 hPa in the EC models, while they are located slightly higher at about 450–400 hPa in the TRMM estimates. Further analysis suggests that these differences in the heating structures between the EC models and the TRMM estimates could be mainly ascribed to the stronger and deeper structures in convective heating components in the EC products than those based on TRMM estimates. Meanwhile, upper-level heating associated with the dipole structure of the stratiform heating component is weaker in the EC products. Regardless of the notable differences in these various datasets, it is encouraging that, after the seasonal mean values are removed from the total heating pattern, the anomalous heating profiles based on these datasets exhibit reasonable agreements with each other over the EEIO as well as over the western Pacific (figure not shown).

Significant differences in the heating structures over the eastern Pacific between the EC models and TRMM estimates are also evident. The heating profiles based on the two EC models display a dipole structure in the vertical, with weak cooling rate above 600 hPa and heating rate below 600 hPa. In contrast, the two TRMM estimates display much stronger cooling effects in the upper troposphere (a factor of 2) than those in EC models. At low levels, the heating structure based on the

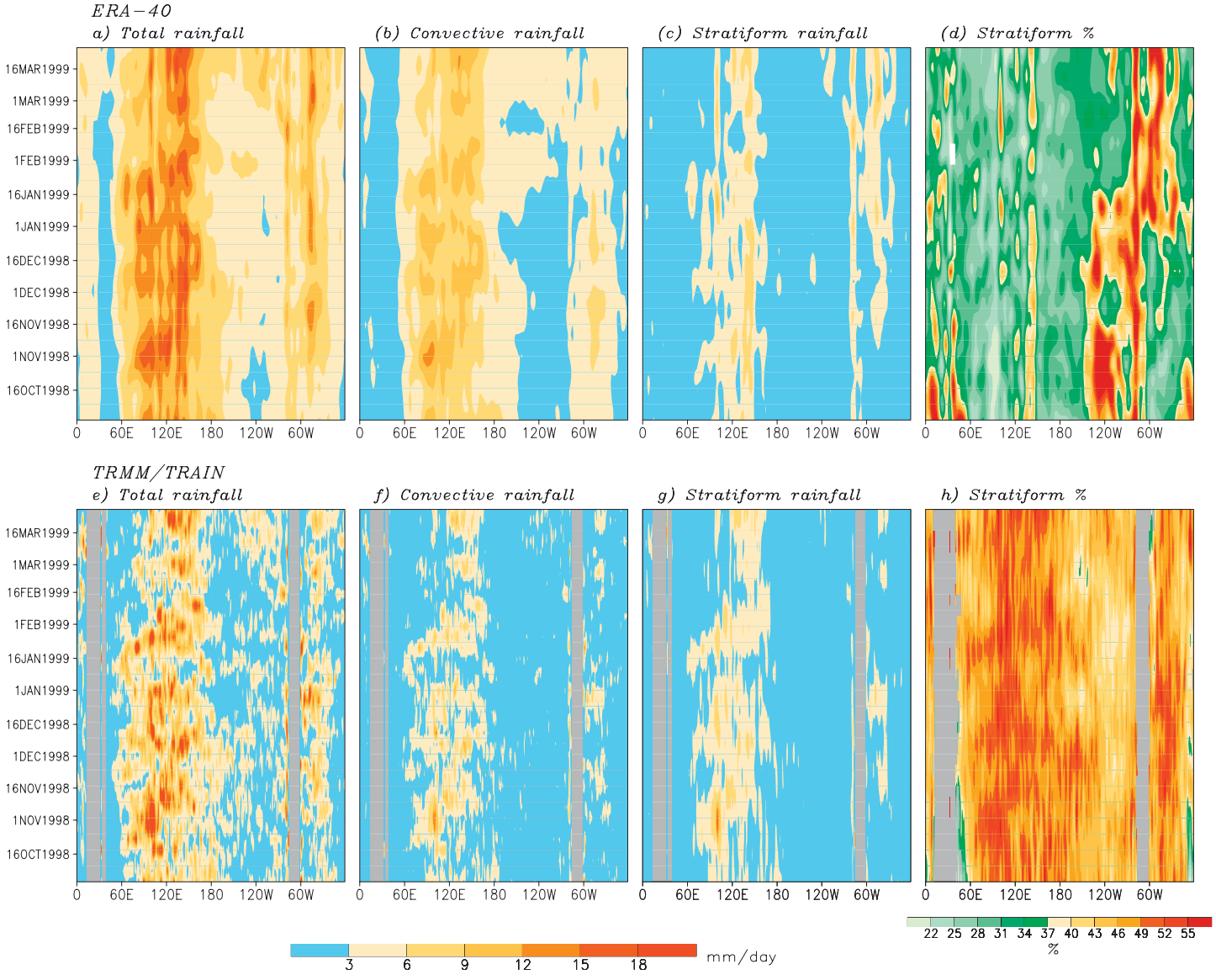

FIG. 9. Hovmöller diagram of (a),(e) total rainfall and its (b),(f) convective and (c),(g) stratiform components, and (d),(h) percentage of stratiform ration during 1998/99 winter based on (top) ERA-40 reanalysis and (bottom) TRMM/TRAIN estimates. All variables are averaged over 10°S–10°N. Shading for rainfall data [(a)–(c),(e)–(g)] is scaled by color bar below (f) (mm day^{-1}). Shading for stratiform percentages [(d),(h)] is scaled by the color bar below (h).

TRMM/TRAIN exhibits some similarity to those by the EC models except in the PBL. In contrast, the TRMM/CSH produces a strong cooling effect throughout the entire troposphere. Maximum heating variability in the eastern Pacific is found in the lower troposphere based on all datasets, in stark contrast to the upper-level heating variability center over the EEIO/western Pacific sector. The heating variability based on the two EC models displays stronger amplitude than those based on two TRMM estimates. It is also noted that two variability centers in the vertical—one at 450 hPa, the other around 750 hPa—are evident in the two TRMM estimates.

Consistent with previous studies based on different data sources, the analysis based on TRMM estimates in the present study affirms that the MJO not only modulates the variations of stratiform rain rate but also its percentage ratio in the total rainfall. Analyses based on the TRMM/TRAIN estimates suggest that the stratiform component has a comparable contribution to the total rain rate as its convective counterpart. Moreover, the partitioning of the stratiform rain can significantly increase (decrease) by more than 5% during the active (undisturbed) MJO phase than the seasonal average percentage. The partitioning of the stratiform component in the total rain rate based on the ERA-40 reanalysis, however, is rather weak (~25%). The strong modulation in the stratiform partition by the MJO as suggested by the TRMM estimate is also not clearly evident based on the ERA-40 product.

When interpreting these differences in the heating and rainfall structures between the EC models and the TRMM estimates, there are a number of caveats that need to be kept in mind. First, there is a sampling issue between the two TRMM estimates. The variables $Q_1 - Q_R$ and Q_1 are generated by TRAIN and CSH algorithms, respectively. In addition, both variables are only computed on grid points where surface rainfall is detected. Thus, in order to facilitate a comparison between these two TRMM estimates, and the TRMM Q_1 estimates are needed to derive an equivalent Q_1 based on both TRAIN $Q_1 - Q_R$ and CSH Q_1. For future developments, standard outputs of the TRMM heating estimates based on different algorithms would be helpful to reduce biases due to these sampling issues. Second, it is also noted that the eddy sensible heat flux [term II in Eq. (1)] is not considered in either TRMM algorithm over nonprecipitating regions, while they are included in the EC models. Thus, comparison of the heating structures between the EC models and the TRMM estimates near the surface should be considered with caution. Third, definitions of the convective and stratiform clouds are different in the EC models and TRMM estimates. In the TRMM estimates, the separation of convective and stratiform precipitation mainly depends on the identification of a "bright band" and a threshold of the reflectivity (e.g., Awaka et al. 1997). In the GCM, while convective precipitation is estimated by the subgrid-scale parameterization scheme, its stratiform counterpart is calculated by considering the condensation due to grid-scale updraft. Thus, the partitioning of convective–stratiform precipitation in the models could be sensitive to the horizontal resolution of the grid system adopted. Fourth, it is also noteworthy that, while the TRMM estimates provide unprecedented benchmarks to validate the current general circulation models, the algorithms on which these estimates are based still heavily depend on high-resolution cloud-resolving models, which are subject to parameterization schemes for subgrid processes in the model.

A goal of this study was to determine the degree these analyses/forecasts and satellite-based data sources might be convergent in their representations of the vertical profiles of latent heating associated with the MJO. The differences in the mean fields are problematic and are associated with remaining uncertainties in the mean precipitation field. Moreover, the differences in the mean vertical structure, particularly in terms of the warm pool versus eastern Pacific, require more research and validation among more analysis products and continued refinements in the satellite-based heating algorithms. In regards to the MJO variations in heating, there is considerably more agreement in at least the magnitude of the variability, and such information can be useful to help constrain models, as the differences in MJO variability exhibited by the models is quite large (Slingo et al. 1996; Zhang et al. 2006; CLIVAR Madden–Julian oscillation Working Group 2009). Similar to the mean fields, there is a fair amount of discrepancy with regards to the depth of the MJO heating variations, and this could have important implications on both the theories and the model performance in terms of propagation characteristics and teleconnection properties. While we have considerable information of the large level of disagreement in MJO-related variations in precipitation, which is suggestive of a similar level of variation in the vertical heating structure; there have been virtually no multimodel comparisons of heating structure properties. Presuming the margin of disagreement is wide, even the level of convergence in these observationally constrained estimates of heating presented here would be quite useful for helping to refine our climate and weather models. A near-term goal of the Climate Variability and Predictability (CLIVAR) MJO Working Group (Sperber and Waliser 2008) and the Year of Tropical Convection (YOTC; Waliser and Moncrieff 2008) is to put more emphasis on such characterizations

and comparisons. In the coming years, the new analyses from ECMWF (ERA-Interim; Simmons et al. 2006), National Aeronautics and Space Administration (NASA) [Modern Era Retrospective-analysis for Research and Applications (MERRA); Bosilovich et al. 2006], and NCEP [Climate Forecast System Reanalysis and Reforecasts (CFSRR; see http://cfs.ncep.noaa.gov)], along with the special products being made available for YOTC, will provide new and even more robust constraints on the various heating structure components so that further improvements in model simulations and forecasts of the MJO can be achieved.

With the above caveats in mind, previous observational studies suggest a transition from shallow to deep convective heating, and then to stratiform heating associated with the MJO evolution (e.g., Lin et al. 2004; Kiladis et al. 2005; Benedict and Randall 2007). However, the vertically tilting features in heating structure are not very evident in either the EC models or the TRMM estimates examined here (e.g., Figs. 5 and 6), although some weak tilting structures can also be discerned associated with the convection as previously mentioned. The weaker vertical tilt in heating structures as shown in the present study, on one hand, could be associated with the differences between radiosonde observations and remote sensing, which was illustrated by Schumacher et al. (2007). On the other hand, this could also be due to the use of 5-day mean heating fields in this study, while subseasonal bandpass-filtered daily data and regression or composite approaches have been employed to achieve the results in the previous studies. In addition, these previous studies have been focused on the western Pacific, while the present study focuses on convective activities over the eastern Indian Ocean. Moreover, the technique by normalizing the heating profiles with surface precipitation rate as employed by Lin et al. (2004) could further make these tilting structures more discernible. In a follow-up study, the heating structures associated with the MJO will be comprehensively examined based on extended periods (e.g., 1998–present) of the satellite retrievals and the new analysis datasets that will become available in the near future.

Acknowledgments. We thank Drs. A. Del Genio and X. Fu and anonymous reviewers for their constructive comments on an earlier version of this manuscript. We also thank W. K.-M. Lau and J. Wu for processing the TRMM/CSH Q_1 datasets. This research was carried out at the Jet Propulsion Laboratory, California Institute of Technology, under a contract with NASA. The TRMM/TRAIN $Q_1 - Q_R$ and Q_R datasets were generated with the support of NASA NEWS research Grants NNG06GC99G and NNG06GC46G, respectively.

REFERENCES

Awaka, J., T. Iguchi, H. Kumagai, and K. Okamoto, 1997: Rain type classification algorithm for TRMM precipitation radar. *Proc. Geoscience and Remote Sensing, 1997/IGARSS '97: Remote Sensing—A Scientific Vision for Sustainable Development,* Singapore, IEEE, 1633–1635.

Bechtold, P., M. Köhler, T. Jung, F. Doblas-Reyes, M. Leutbecher, M. J. Rodwell, F. Vitart, and G. Balsamo, 2008: Advances in simulating atmospheric variability with the ECMWF model: From synoptic to decadal time-scales. *Quart. J. Roy. Meteor. Soc.,* **134,** 1337–1351.

Benedict, J. J., and D. A. Randall, 2007: Observed characteristics of the MJO relative to maximum rainfall. *J. Atmos. Sci.,* **64,** 2332–2354.

Bosilovich, M. G., and Coauthors, 2006: NASA's modern era retrospective-analysis for research and applications. *U.S. CLIVAR Variations,* No. 4, U.S. CLIVAR Project Office, Washington, DC, 5–8.

Chan, S. C., and S. Nigam, 2009: Residual diagnosis of diabatic heating from ERA-40 and NCEP reanalyses: Intercomparisons with TRMM. *J. Climate,* **22,** 414–428.

Chang, C.-P., and H. Lim, 1988: Kelvin wave-CISK: A possible mechanism for the 30–50-day oscillations. *J. Atmos. Sci.,* **45,** 1709–1720.

Chen, Y. H., and A. D. Del Genio, 2009: Evaluation of tropical cloud regimes in observations and a general circulation model. *Climate Dyn.,* **32,** 355–369.

Cho, H. R., and D. Pendlebury, 1997: Wave CISK of equatorial waves and the vertical distribution of cumulus heating. *J. Atmos. Sci.,* **54,** 2429–2440.

CLIVAR Madden–Julian Oscillation Working Group, 2009: MJO simulation diagnostics. *J. Climate,* **22,** 3006–3030.

Emanuel, K. A., 1987: An air–sea interaction model of intraseasonal oscillations in the tropics. *J. Atmos. Sci.,* **44,** 2324–2340.

Fu, X., and B. Wang, 2009: Critical roles of the stratiform rainfall in sustaining the Madden–Julian oscillation: GCM experiments. *J. Climate,* **22,** 3939–3959.

Grecu, M., and W. S. Olson, 2006: Bayesian estimation of precipitation from satellite passive microwave observations using combined radar–radiometer retrievals. *J. Appl. Meteor. Climatol.,* **45,** 416–433.

——, ——, C. L. Shie, T. S. L'Ecuyer, and W.-K. Tao, 2009: Combining satellite microwave radiometer and radar observations to estimate atmospheric heating profiles. *J. Climate,* in press.

Hendon, H. H., and B. Liebmann, 1990: The intraseasonal (30–50 day) oscillation of the Australian summer monsoon. *J. Atmos. Sci.,* **47,** 2909–2924.

——, and M. L. Salby, 1994: The life cycle of the Madden–Julian oscillation. *J. Atmos. Sci.,* **51,** 2225–2237.

Higgins, R. W., and W. Shi, 2001: Intercomparison of the principal modes of interannual and intraseasonal variability of the North American monsoon system. *J. Climate,* **14,** 403–417.

Houze, R. A., 1982: Cloud clusters and large-scale vertical motions in the tropics. *J. Meteor. Soc. Japan,* **60,** 396–410.

Huffman, G. J., and Coauthors, 2007: The TRMM Multisatellite Precipitation Analysis (TMPA): Quasi-global, multiyear, combined-sensor precipitation estimates at fine scales. *J. Hydrometeor.,* **8,** 38–55.

Janiskova, M., J. F. Mahfouf, J. J. Morcrette, and F. Chevallier, 2002: Linearized radiation and cloud schemes in the ECMWF

model: Development and evaluation. *Quart. J. Roy. Meteor. Soc.,* **128,** 1505–1527.

Jiang, X., D. E. Waliser, M. C. Wheeler, C. Jones, M. N. Lee, and S. D. Schuert, 2008: Assessing the skill of an all-season statistical forecast model for the Madden–Julian oscillation. *Mon. Wea. Rev.,* **136,** 1940–1956.

Johnson, R. H., T. M. Rickenbach, S. A. Rutledge, P. E. Ciesielski, and W. H. Schubert, 1999: Trimodal characteristics of tropical convection. *J. Climate,* **12,** 2397–2418.

Kemball-Cook, S. R., and B. C. Weare, 2001: The onset of convection in the Madden–Julian oscillation. *J. Climate,* **14,** 780–793.

Kessler, W. S., and R. Kleeman, 2000: Rectification of the Madden–Julian oscillation into the ENSO cycle. *J. Climate,* **13,** 3560–3575.

Kikuchi, K., and Y. N. Takayabu, 2004: The development of organized convection associated with the MJO during TOGA COARE IOP: Trimodal characteristics. *Geophys. Res. Lett.,* **31,** L10101, doi:10.1029/2004GL019601.

Kiladis, G. N., K. H. Straub, and P. T. Haertel, 2005: Zonal and vertical structure of the Madden–Julian oscillation. *J. Atmos. Sci.,* **62,** 2790–2809.

Kim, D., and Coauthors, 2009: Application of MJO simulation diagnostics to climate models. *J. Climate,* in press.

Kuang, Z., 2008: A moisture-stratiform instability for convectively coupled waves. *J. Atmos. Sci.,* **65,** 834–854.

Lau, K.-M., and P. H. Chan, 1986: Aspects of the 40–50-day oscillation during the northern summer as inferred from outgoing longwave radiation. *Mon. Wea. Rev.,* **114,** 1354–1367.

——, and L. Peng, 1987: Origin of low-frequency (intraseasonal) oscillations in the tropical atmosphere. Part I: Basic theory. *J. Atmos. Sci.,* **44,** 950–972.

Lau, W. K.-M., and D. E. Waliser, 2005: *Intraseasonal Variability in the Atmosphere–Ocean Climate System*. Springer, 474 pp.

L'Ecuyer, T. S., and G. L. Stephens, 2003: The tropical oceanic energy budget from the TRMM perspective. Part I: Algorithm and uncertainties. *J. Climate,* **16,** 1967–1985.

——, and ——, 2007: The tropical atmospheric energy budget from the TRMM perspective. Part II: Evaluating GCM representations of the sensitivity of regional energy and water cycles to the 1998–99 ENSO cycle. *J. Climate,* **20,** 4548–4571.

——, and G. McGarragh, 2009: A 10-year climatology of tropical radiative heating and its vertical structure from TRMM observations. *J. Climate,* in press.

Li, J. L., J. H. Jiang, D. E. Waliser, and A. M. Tompkins, 2007: Assessing consistency between EOS MLS and ECMWF analyzed and forecast estimates of cloud ice. *Geophys. Res. Lett.,* **34,** L08701, doi:10.1029/2006GL029022.

Liebmann, B., and D. L. Hartmann, 1984: An observational study of tropical–midlatitude interaction on intraseasonal time scales during winter. *J. Atmos. Sci.,* **41,** 3333–3350.

Lin, J.-L., B. Mapes, M. Zhang, and M. Newman, 2004: Stratiform precipitation, vertical heating profiles, and the Madden–Julian oscillation. *J. Atmos. Sci.,* **61,** 296–309.

——, and Coauthors, 2006: Tropical intraseasonal variability in 14 IPCC AR4 climate models. Part I: Convective signals. *J. Climate,* **19,** 2665–2690.

Lin, X., and R. H. Johnson, 1996: Heating, moistening, and rainfall over the western Pacific warm pool during TOGA COARE. *J. Atmos. Sci.,* **53,** 3367–3383.

Madden, R. A., and P. R. Julian, 1994: Observations of the 40–50-day tropical oscillation—A review. *Mon. Wea. Rev.,* **122,** 814–837.

Mahfouf, J. F., 1999: Influence of physical processes on the tangent-linear approximation. *Tellus,* **51A,** 147–166.

Majda, A. J., and S. N. Stechmann, 2009: The skeleton of tropical intraseasonal oscillations. *Proc. Natl. Acad. Sci. USA,* **106,** 8417–8422.

Maloney, E. D., and D. L. Hartmann, 2000: Modulation of eastern North Pacific hurricanes by the Madden–Julian oscillation. *J. Climate,* **13,** 1451–1460.

Mapes, B. E., 2000: Convective inhibition, subgrid-scale triggering energy, and stratiform instability in a toy tropical wave model. *J. Atmos. Sci.,* **57,** 1515–1535.

McPhaden, M. J., 1999: Genesis and evolution of the 1997-98 El Niño. *Science,* **283,** 950–954.

Mo, K. C., 2000: Intraseasonal modulation of summer precipitation over North America. *Mon. Wea. Rev.,* **128,** 1490–1505.

Moore, A. M., and R. Kleeman, 1999: Stochastic forcing of ENSO by the intraseasonal oscillation. *J. Climate,* **12,** 1199–1220.

Morita, J., Y. N. Takayabu, S. Shige, and Y. Kodama, 2006: Analysis of rainfall characteristics of the Madden–Julian oscillation using TRMM satellite data. *Dyn. Atmos. Oceans,* **42,** 107–126.

Neelin, J. D., I. M. Held, and K. H. Cook, 1987: Evaporation–wind feedback and low-frequency variability in the tropical atmosphere. *J. Atmos. Sci.,* **44,** 2341–2348.

Olson, W. S., C. D. Kummerow, Y. Hong, and W.-K. Tao, 1999: Atmospheric latent heating distributions in the tropics derived from satellite passive microwave radiometer measurements. *J. Appl. Meteor.,* **38,** 633–664.

Peixoto, J. P., and A. H. Oort, 1992: *Physics of Climate*. Springer, 564 pp.

Rabier, F., J. N. Thepaut, and P. Courtier, 1998: Extended assimilation and forecast experiments with a four-dimensional variational assimilation system. *Quart. J. Roy. Meteor. Soc.,* **124,** 1861–1887.

Schumacher, C., M. H. Zhang, and P. E. Ciesielski, 2007: Heating structures of the TRMM field campaigns. *J. Atmos. Sci.,* **64,** 2593–2610.

Shige, S., Y. N. Takayabu, W.-K. Tao, and D. E. Johnson, 2004: Spectral retrieval of latent heating profiles from TRMM PR data. Part I: Development of a model-based algorithm. *J. Appl. Meteor.,* **43,** 1095–1113.

Simmons, A., S. Uppala, D. Dee, and S. Kobayashi, 2006: ERA-Interim: New ECMWF reanalysis products from 1989 onwards. *ECMWF Newsletter,* No. 110, ECMWF, Reading, United Kingdom, 25–35.

Slingo, J. M., 1987: The development and verification of a cloud prediction scheme for the ECMWF model. *Quart. J. Roy. Meteor. Soc.,* **113,** 899–927.

——, and Coauthors, 1996: Intraseasonal oscillations in 15 atmospheric general circulation models: Results from an AMIP diagnostic subproject. *Climate Dyn.,* **12,** 325–357.

——, P. M. Inness, and K. R. Sperber, 2005: Modeling. *Intraseasonal Variability in the Atmosphere–Ocean Climate System,* W. K. M. Lau and D. E. Waliser, Eds., Springer, 361–388.

Sperber, K. R., 2003: Propagation and the vertical structure of the Madden–Julian oscillation. *Mon. Wea. Rev.,* **131,** 3018–3037.

——, and D. E. Waliser, 2008: New approaches to understanding, simulating, and forecasting the Madden–Julian oscillation. *Bull. Amer. Meteor. Soc.,* **89,** 1917–1920.

Sui, C.-H., and K.-M. Lau, 1989: Origin of low-frequency (intraseasonal) oscillations in the tropical atmosphere. Part II: Structure and propagation of mobile wave-CISK modes and their modification by lower boundary forcings. *J. Atmos. Sci.,* **46,** 37–56.

Takahashi, M., 1987: A theory of the slow phase speed of the intraseasonal oscillation using the wave-CISK. *J. Meteor. Soc. Japan,* **65,** 43–49.

Tao, W.-K., S. Lang, J. Simpson, and R. Adler, 1993a: Retrieval algorithms for estimating the vertical profiles of latent-heat release—Their applications for TRMM. *J. Meteor. Soc. Japan,* **71,** 685–700.

——, J. Simpson, C. H. Sui, B. Ferrier, S. Lang, J. Scala, M. D. Chou, and K. Pickering, 1993b: Heating, moisture, and water budgets of tropical and midlatitude squall lines: Comparisons and sensitivity to longwave radiation. *J. Atmos. Sci.,* **50,** 673–690.

——, S. Lang, J. Simpson, W. S. Olson, D. Johnson, B. Ferrier, C. Kummerow, and R. Adler, 2000: Vertical profiles of latent heat release and their retrieval for TOGA COARE convective systems using a cloud resolving model, SSM/I, and ship-borne radar data. *J. Meteor. Soc. Japan,* **78,** 333–355.

——, and Coauthors, 2001: Retrieved vertical profiles of latent heat release using TRMM rainfall products for February 1988. *J. Appl. Meteor.,* **40,** 957–982.

——, and Coauthors, 2006: Retrieval of latent heating from TRMM measurements. *Bull. Amer. Meteor. Soc.,* **87,** 1555–1572.

Tian, B., and V. Ramanathan, 2002: Role of tropical clouds in surface and atmospheric energy budget. *J. Climate,* **15,** 296–305.

——, G. J. Zhang, and V. Ramanathan, 2001: Heat balance in the Pacific warm pool atmosphere during TOGA COARE and CEPEX. *J. Climate,* **14,** 1881–1893.

——, D. E. Waliser, E. J. Fetzer, B. H. Lambrigtsen, Y. L. Yung, and B. Wang, 2006: Vertical moist thermodynamic structure and spatial-temporal evolution of the MJO in AIRS observations. *J. Atmos. Sci.,* **63,** 2462–2485.

——, Y. L. Yung, D. E. Waliser, T. Tyranowski, L. Kuai, E. J. Fetzer, and F. W. Irion, 2007: Intraseasonal variations of the tropical total ozone and their connection to the Madden-Julian Oscillation. *Geophys. Res. Lett.,* **34,** L08704, doi:10.1029/2007GL029451.

——, and Coauthors, 2008: Does the Madden-Julian oscillation influence aerosol variability? *J. Geophys. Res.,* **113,** D12215, doi:10.1029/2007JD009372.

Tiedtke, M., 1993: Representation of clouds in large-scale models. *Mon. Wea. Rev.,* **121,** 3040–3061.

Tokioka, T., K. Yamazaki, A. Kitoh, and T. Ose, 1988: The equatorial 30–60 day oscillation and the Arakawa–Schubert penetrative cumulus parameterization. *J. Meteor. Soc. Japan,* **66,** 883–901.

Uppala, S. M., and Coauthors, 2005: The ERA-40 re-analysis. *Quart. J. Roy. Meteor. Soc.,* **131,** 2961–3012.

Waliser, D. E., and M. Moncrieff, 2008: The Year of Tropical Convection (YOTC) Science Plan: A joint WCRP–WWRP/THORPEX International Initiative. WMO/TD 1452, WCRP 130, WWRP/THORPEX 9, WMO, Geneva, Switzerland, 26 pp.

——, R. Murtugudde, P. Strutton, and J. L. Li, 2005: Subseasonal organization of ocean chlorophyll: Prospects for prediction based on the Madden-Julian Oscillation. *Geophys. Res. Lett.,* **32,** L23602, doi:10.1029/2005GL024300.

——, and Coauthors, 2006: The Experimental MJO Prediction Project. *Bull. Amer. Meteor. Soc.,* **87,** 425–431.

Wang, B., 2005: Theories. *Intraseasonal Variability in the Atmosphere-Ocean Climate System,* W. K. M. Lau and D. E. Waliser, Eds., Springer, 389–424.

——, and H. Rui, 1990: Dynamics of the coupled moist Kelvin–Rossby wave on an equatorial β-plane. *J. Atmos. Sci.,* **47,** 397–413.

Weickmann, K. M., 1983: Intraseasonal circulation and outgoing longwave radiation modes during Northern Hemisphere winter. *Mon. Wea. Rev.,* **111,** 1838–1858.

Yanai, M., S. Esbensen, and J.-H. Chu, 1973: Determination of bulk properties of tropical cloud clusters from large-scale heat and moisture budgets. *J. Atmos. Sci.,* **30,** 611–627.

Zhang, C., 2005: Madden-Julian Oscillation. *Rev. Geophys.,* **43,** RG2003, doi:10.1029/2004RG000158.

——, M. Dong, S. Gualdi, H. H. Hendon, E. D. Maloney, A. Marshall, K. R. Sperber, and W. Wang, 2006: Simulations of the Madden-Julian oscillation in four pairs of coupled and uncoupled global models. *Climate Dyn.,* **27,** 573–592.